https://doi.org/10.1016/S1872-2067(22)64166-4

High-Entropy Alloy Metallene for Highly Efficient Overall Water Splitting in Acidic Media

Dan Zhang[1,2], Yue Shi[1], Xilei Chen[2], Jianping Lai[1,] Bolong Huang[3,]* and Lei Wang[1,2]**

[1] Key Laboratory of Eco-chemical Engineering, Ministry of Education, Taishan scholar advantage and characteristic discipline team of Eco-chemical process and technology, Laboratory of Inorganic Synthesis and Applied Chemistry, College of Chemistry and Molecular Engineering, Qingdao University of Science and Technology, Qingdao 266042, P. R. China,

[2] Shandong Engineering Research Center for Marine Environment Corrosion and Safety Protection, College of Environment and Safety Engineering, Qingdao University of Science and Technology, Qingdao 266042, P. R. China

[3] Department of Applied Biology and Chemical Technology, The Hong Kong Polytechnic University, Hung Hom, Kowloon, Hong Kong SAR, China

E-mail: inorchemwl@126.com; bhuang@polyu.edu.hk; jplai@qust.edu.cn

Abstract: The development of acid-stable electrocatalysts at high current density for overall water splitting is crucial for achieving high-performance electrolyzers. Herein, we successfully prepared IrPdRhMoW HEA metallene with rich amorphous and crystalline structures as an efficient bifunctional electrocatalyst for water splitting under acidic conditions through a simple low-temperature oil phase method for the first time. In 0.5 M H_2SO_4, the overpotentials for hydrogen evolution reaction (HER) and oxygen evolution reaction (OER) of IrPdRhMoW/C at a current density of 10 mA cm^{-2} are 15 mV and 188 mV, respectively, far exceeding the commercial Pt/C (47 mV) and RuO_2 (305 mV). Using IrPdRhMoW/C for the overall water splitting, only a cell voltage of 1.48 V is required to achieve a current density of 10 mA cm^{-2}. More importantly, the IrPdRhMoW/C still maintains excellent electroactivity and structural stability after 500 hours of water splitting at a high current density of 100 mA cm^{-2}. Density functional theory (DFT) calculations reveal the self-balanced effect of electronic structures in the HEA due to the co-existence of crystalline and amorphous lattice structures. The strong orbital couplings not only maximize the electroactivity towards both HER and OER but also stabilize the valence states of metal sites for durable electrocatalysis.

Introduction

The proton exchange membrane water electrolyzer (PEMWE) provides a new direction for the development of new generation of electrolyzers due to its high efficiency and power density at low temperature.[1-4] In the process of electrolysis of water, the design of efficient and stable hydrogen evolution (HER) and oxygen evolution (OER) catalysts is the premise to further improve the application of electrolyzers.[5-7] Based on HER and OER volcano-shaped distribution curves, the precious metals (Ir, Ru etc.) are the dominant benchmark electrocatalysts.[8-11] For acidic overall water splitting, Ir-based and Ru-based bifunctional catalysts are still the most common choices.[12-16] However, the high dissolution rate of Ru-based catalysts under acidic conditions leads to rapid deactivation of the catalysts, which greatly reduces its practical application value.[17-19] Similarly, Ir-based materials still face the challenges of low mass activity and limited stability under high current density for acidic overall water splitting. All these issues make these electrocatalysts fail to meet the application requirements of PEMWE (the overpotential at 100 mA cm^{-2} is more than 420 mV, and the stability under high current density is less than 120 h for acidic overall water splitting).[20-22] Therefore, developing novel electrocatalyst with both excellent electroactivity and stability are the urgent tasks.

High-entropy alloys (HEAs) composed of at least five elements have drawn intense research interest in recent years due to their strong tolerance under extreme conditions, which is induced by high entropy effect and sluggish diffusion.[23-26] Meanwhile, the controllability of different components also play significant roles in boosting the catalysis process.[27-30] From a crystal phase point of view, catalysts with amorphous/crystalline interfaces tend to have excellent catalytic performance due to the abundant uncoordinated active sites exposed by the amorphous components and the unique atomic arrangement of the crystalline components.[31-33] Besides, the synergistic effect of different crystal phases can improve the electroactivity and modulate the interaction between active sites and reaction intermediates.[22,31,34-36] In addition, the amorphous structure with flexible coordination environments can promote self-regulation and alleviation of structural disturbance during the catalysis process, thereby improving the stability of catalysts.[31,37] In terms of morphology, metallenes have the advantages of large surface metal atomic volume ratio, abundant surface metal defects, and excellent stability, hence exhibiting brilliant catalytic performance.[38-43] Therefore, it is expected that the electrocatalyst combine the advantages of rich amorphous/crystalline interfaces, the synergistic effect of HEA and the metallene structure will be promising solution to the electrocatalyst design for acidic water splitting.

In this work, we successfully prepared IrPdRhMoW HEA metallene (average thickness of only~1.9 nm) with rich amorphous/crystalline phase boundaries through a simple low-temperature oil phase approach for the first time. In 0.5 M H_2SO_4, IrPdRhMoW/C exhibits unprecedented catalytic activity and stability for overall water splitting. Density functional theory (DFT) calculations have demonstrated that the existence of amorphous lattice structure has benefited the electroactivity activation in the crystalline lattice structure. The strong orbital coupling among different metal sites induces the self-balanced effect, which promotes the site-to-site electron transfer and enhances the stability of HEA during electrocatalysis.

Results and Discussion

A simple one-pot wet-chemical method was used to prepare HEA metallene with oleylamine as the solvent. Among them, carbonyl molybdenum ($Mo(CO)_6$) and carbonyl tungsten ($W(CO)_6$) are not only metal precursors, but also capping agents and reducing agents because carbonyl groups can be decomposed to generate CO at high temperature.[44] As shown in **Fig. 1a**, the transmission electron microscopy (TEM) image of the HEA metallene shows a distinct morphology of ultrathin nanosheets. Further test data from atomic force microscopy (AFM) reveals that the thickness of the ultrathin nanosheets was only 1.9 nm (**Supplementary Fig. 1**). The characteristic peaks of the X-ray diffraction (XRD) pattern correspond to the standard peaks of Pd (JCPDS No. 46-1043) (**Fig. 1b**), indicating that the elements in HEA metallene are arranged based on the face-centered cubic (fcc) structure. And the wider peak shape echoes the ultrathin characteristics of the material. The negatively shifted peak positions also precisely account for alloy formation.[23] Furthermore, the presence of a big drum in the range of 20° to 30° indicates low crystallinity and the possible existence of amorphous structural components in the prepared HEA metallene. Further high-resolution TEM (HRTEM) image (**Fig. 1c**) clearly showed distinct crystalline and amorphous parts, as well as a large number of grain boundaries. The lattice spacing of the crystalline part is 0.225 nm, which matches the XRD pattern. In addition, abundant atomic steps can be identified through the HRTEM image of the edge portion in the ultrathin metallene (**Fig. 1d**), and clear metal defects can also be found after fast Fourier transform (FFT) (**Supplementary Fig. 2**). Subsequent, density functional theory (DFT) calculations indicate that the defect site is likely to be Mo. All the evidence shows that the prepared HEA has a unique structure of ultrathin metallene. In order to explore the elemental composition of the HEA, the high-angle annular dark-field scanning TEM (HAADF-STEM) and energydispersive X-ray spectroscopy (EDS) element mapping were carried out. **Fig. 1e** clearly shows the evenly distributions of Ir, Pd, Rh, Mo, W, and the composition ratio is about Ir:Pd:Rh:Mo:W= 25.4:32.1:29.7:7.5:5.3, matching with the result of inductively coupled plasma atomic emission

spectrometer (ICP-AES). The thermodynamic parameters of the IrPdRhMoW HEA metallene were further calculated.[45] The atomic size difference (δ) of the material is 14.7%, much larger than 6.5%. At the same time, the mixing enthalpy (ΔH_{mix}) of the system is -55.83 KJ mol^{-1}. Both data show that the IrPdRhMoW HEA metallene has a great tendency to form an amorphous phase which agrees with the HRTEM image.

The X-ray photoelectron spectroscopy (XPS) spectra of IrPdRhMoW also prove the existence of five elements, and further explored the electronic structures of each element. As shown in **Supplementary Fig. 3a**, the characteristic peaks at 60.7 eV and 63.8 eV are assigned to Ir^0 $4f_{7/2}$ and Ir^0 $4f_{5/2}$, and the small oxidation peaks (61.7 eV and 64.9 eV) are due to surface oxidation. In the spectrum of Pd (**Supplementary Fig. 3b**), the characteristic peaks located at 335.5 eV and 340.7 eV are assigned to Pd^0 $3d_{5/2}$ and Pd^0 $3d_{3/2}$, respectively. And the characteristic peaks located at 307.2 eV and 312.1 eV are assigned to Rh^0 $3d_{5/2}$ and Rh^0 $3d_{3/2}$ (**Supplementary Fig. 3c**). In **Supplementary Fig. 3d** and **3e**, the analysis of Mo and W spectra indicates the coexistence of metallic state and oxidation state.

To evaluate the electrochemical performance of the synthesized HEA metallene, we evaluated the catalyst for water splitting under acidic conditions via a three-electrode system. The iR-compensated linear sweep voltammetry (LSV) curve (**Fig. 2a**) shows the excellent HER catalytic activity of IrPdRhMoW/C with an overpotential of only 15 mV at 10 mA cm^{-2} in 0.5 M H_2SO_4, far exceeding the commercial Pt/C (47 mV) (**Fig. 2b**) and most catalysts published in recent years (**Supplementary Table 1**). The large exchange current density (2.5 mA cm^{-2}) and small Tafel slope (15 mV dec^{-1}) of IrPdRhMoW/C also reflect intrinsically faster HER kinetics (**Fig. 2c** and **2d**). Meanwhile, the turnover frequency (TOF) value of IrPdRhMoW/C (34.7 s^{-1} at 100 mV) is 2.7 times larger than the commercial Pt/C, indicating a higher intrinsic activity of the catalyst than other acidic HER catalysts reported in recent years (**Fig. 2e, Supplementary Table 2**). The superior performances are attributed to the large exposed unsaturated sites at the crystalline/amorphous interface, which sigificantly enhances the intrinsic activity of the catalyst. Then, the cyclic voltammetry (CV) curves (**Supplementary Fig. 4**) at different scan rates deduced that the catalyst possesses a large double layer capacitance (C_{dl}) (8.0 mF cm^{-2}), which reveals a considerable electrochemically active area (**Fig. 2f**). Moreover, the electrochemical active surface area (ECSA) of the catalysts were also estimated by using the copper underpotential deposition (Cu-UPD) method (**Supplementary Fig. 5**). By calculation, the ECSA of IrPdRhMoW/C is about 132.0 cm^2/g, which is much larger than that of Pt/C (73.8 cm^2/g) (**Supplementary Fig. 6**). We speculate that the ultrathin 2D metallene structure benefits the such a large ECSA in IrPdRhMoW/C. The reaction kinetics were

investigated using electrochemical impedance spectroscopy (EIS) (**Supplementary Fig. 7**). Obviously, IrPdRhMoW/C has a small resistance value (~5.2 Ω), which indicates that IrPdRhMoW/C has strong charge transfer kinetics. Furthermore, the stability of IrPdRhMoW/C was evaluated by CV cycling and chronoamperometric (i-t) test (**Supplementary Fig. 8**). After 10000 CV cycles, the polarization curve of IrPdRhMoW/C exhibits a slight decay (**Supplementary Fig. 8a**). The i-t test of IrPdRhMoW/C shows negligible loss of current density even after 50 h (**Supplementary Fig. 8b**). The above durability tests jointly verify the excellent stability of IrPdRhMoW/C. The structural information of IrPdRhMoW/C after HER electrocatalysis was further studied. Satisfyingly, the IrPdRhMoW/C still maintains the morphology of the metallene with limited change in structure and composition as proved by structure characterizations by TEM, XRD and XPS (**Supplementary Fig. 9 and 10**). Consequently, from the perspective of morphology, structure, and catalytic activity, IrPdRhMoW/C exhibits excellent stability during the HER process.

The anode OER performance of IrPdRhMoW/C was also effectively evaluated (**Fig. 3a**). The overpotential of IrPdRhMoW/C is 188 mV at 10 mA cm^{-2}, which is significantly lowered when compared to the commercial RuO_2 (305 mV) (**Fig. 3b**), even outperforming other recently reported OER catalysts in acidic electrolytes (**Supplementary Table 3**). Additionally, the mass activity of IrPdRhMoW/C at 266 mV is up to 3.67 A $mg^{-1}_{noble\ metal}$, which is much higher than previously reported state-of-the-art acidic OER electrocatalysts (**Supplementary Fig. 11**). Furthermore, its Tafel slope of 60 mV dec^{-1} is also smaller than the commercial RuO_2 (125 mV dec^{-1}) (**Fig. 3c**), indicating its excellent OER kinetics. And the TOF value at 300 mV is 7.4 s^{-1} (**Fig. 3d**), outperforming most catalysts (**Supplementary Table 3**). The small impedance value further indicates that IrPdRhMoW/C has advanced OER kinetics (**Fig. 3e**). In the stability test, the LSV decays only slightly after 10000 CV cycles (**Fig. 3f**), while its 50 hours i-t test shows a negligible decrease in activity (**Supplementary Fig. 12**). According to previously reported literature, the main active phase of the catalyst during the OER reaction under acidic conditions is oxide.[46,47] So we further carried out the structural characterization of the catalyst after stability test. It was found by XRD pattern that the characteristics of the alloy properties were weakened (**Supplementary Fig. 13**). Then, the information of each element was characterized by XPS spectra. As shown in **Supplementary Fig. 14**, the characteristic peaks of metal Pd and Rh do not change significantly, the oxidation peak of Ir is significantly enhanced, and metal W and Mo also undergo obvious oxidation during the OER process. It is suggested that the metal oxides of Ir, Mo and W in the HEA play a major role in the OER process.

To investigate the origins of high electroactivity of the IrPdRhMoW HEA, we further applied the DFT calculations. As the experimental characterizations, the IrPdRhMoW HEA is constructed by both crystalline and amorphous lattice (**Fig. 4a**). After relaxation, the surface structure of the crystalline part has shown some evident distortion while the amorphous part displays an uneven surface with abundant low-coordinated sites. The bonding and anti-bonding sites near the Fermi level (E_F) are mostly dominated by Ir, Pd, Rh and Mo, W, respectively (**Fig. 4b**). In particular, we notice the distorted surfaces of IrPdRhMoW HEA exhibit the electron-rich feature to guarantee efficient electron transfer. The projected partial density of states (PDOSs) reveals the strong orbital coupling pairs, where Pd-4d, Rh-4d, and Ir-5d orbitals have well overlapped with each other (**Fig. 4c**). Meanwhile, the Mo-4d and W-5d orbitals also show highly similar orbital patterns with strong overlapping. Such orbital coupling not only enhances the electroactivity but also improves the robustness of the electronic structure to realize durable electrocatalysis in the acid environment. The radial distribution function (RDF) of the IrPdRhMoW HEA has been simulated and compared with the highly crystalline IrPdRhMoW structures (**Fig. 4d**). Notably, the IrPdRhMoW HEA has shown the weakened peaks for the first peak and the following peaks become broadened and blurred, supporting the co-existence of crystalline and amorphous parts in the lattice structure. Then, the site-independent PDOS further demonstrates the self-balanced electronic structures in IrPdRhMoW HEA. It is noted that the Pd-4d sites show a gradual upshifting trend from the crystalline part to the amorphous part (**Fig. 4e**). This indicates that the amorphous part in IrPdRhMoW HEA is critical to supply highly electroactive sites to reach efficient OER and HER. The mixture of crystalline and amorphous structure has led to the self-balanced effect in the Rh-4d and Ir-5d orbitals (**Fig. 4f**). For the crystalline part, the e_g-t_{2g} splitting in Rh-4d shows an enlarged trend while the amorphous part demonstrates the opposite trend. Such an opposite evolution guarantees the highly robust electroactivity and stability of Rh sites. Interestingly, the self-balanced effect in Ir-5d delivers a reverse trend, where the e_g-t_{2g} splitting are alleviated in the crystalline part but enlarged in the amorphous part (**Fig. 4g**). The self-balanced effect in Rh-4d and Ir-5d enables the activation of both crystalline and amorphous parts in the structure to maximize the electroactivity. In contrast, the Mo-4d orbitals deliver a similar downshifting towards the E_F to facilitate the site-to-site electron transfer (**Fig. 4h**). The W-5d orbitals also show the self-balanced effect to supply the protection to Pd-4d, Rh-4d, and Ir-5d orbitals to maintain robust valence states for the electrocatalysis (**Fig. 4i**). For the metal vacancies, all the metals display the negative formation energies, indicating the abundant metal vacancies as experimental results (**Fig. 4j**). In comparison, the vacancies of W show the lowest formation energy while the other metals demonstrate

similar formation energies. The reaction energies of OER show a continuous uphill trend under the U = 0 V, where the largest barrier of 1.41 eV occurs at the conversion from O* towards OOH* as the rate-determining step (RDS) (**Fig. 4k**). With the applied potential of equilibrium potential of 1.23 V, the overpotential for OER is estimated to be 0.18 V, which agrees well with the electrochemical tests (**Fig. 4l**). Meanwhile, for the acidic HER process, all the metals sites have displayed much more optimal adsorption energies of proton than the pure Pd surface (**Fig. 4m**). The overbinding effects on the pristine Pd surfaces have been significantly suppressed. These results indicate that the overall electroactivity towards HER has been achieved due to the self-balanced effect of electronic structures in the IrPdRhMoW HEA.

In view of the remarkable bifunctional catalytic properties of IrPdRhMoW/C for acidic HER and OER, the catalyst ink was drop-coated on carbon paper (CP) (0.2 mg cm^{-2}), and then the IrPdRhMoW/CP was used as both cathode and anode electrodes to assemble double electrodes electrolytic cell (**Fig. 5a**). IrPdRhMoW/CP requires only a low voltage of 1.48 V at 10 mA cm^{-2} and 1.59 V for 100 mA cm^{-2}, which is superior to that of Pt-C/CP||RuO_2/CP-based electrolyzers (1.59 V at 10 mA cm^{-2}) (**Fig. 5b**), and reported acidic electrocatalysts (**Supplementary Table 4**). In addition, IrPdRhMoW/CP||IrPdRhMoW/CP shows high Faradaic efficiencies of HER and OER close to 100%, and the volume ratio of hydrogen and oxygen is 2:1 (**Fig. 5c**), indicating that IrPdRhMoW/C has excellent electron utilization. Furthermore, IrPdRhMoW/CP||IrPdRhMoW/CP also shows excellent stability during 500 hours of continuous overall water splitting at 100 mA cm^{-2} (**Fig. 5d and Supplementary Fig. 15**), which also sets a record for the stability of acidic water splitting catalysts at relatively high current density (**Supplementary Table 5**).

Conclusion

In conclusion, we successfully prepared IrPdRhMoW HEA metallene with abundant amorphous structures as robust electrocatalysts for overall water splitting under acidic conditions by a simple oil-phase synthesis method for the first time. In 0.5 M H_2SO_4, at a current density of 10 mA cm^{-2}, the HER and OER overpotentials of IrPdRhMoW/C are 15 mV and 188 mV, respectively. The excellent intrinsic activity values (34.7 H_2 s^{-1} and 7.4 O_2 s^{-1}) reveal the superior catalytic activity of the HEA metallene. In addition, the overall water splitting also requires only a cell voltage of 1.48 V for 10 mA cm^{-2} and 1.59 V for 100 mA cm^{-2}, outperforming most reported bifunctional electrocatalyst. IrPdRhMoW/C maintains outstanding catalytic performance and structural stability after 500 hours of continuous overall water splitting under 100 mA cm^{-2}. DFT calculations have indicated that the self-balanced electronic structure in HEA has

supplied improved the electroactivity of the HEA due to the interactions between amorphous and crystalline lattice structures. Due to the improved electroactivity, HEA displays the efficient HER and OER with low energy barriers and long stability. This work not only successfully prepared HEAs metallenes for the first time, but also developed the charge self-balanced effect to solve the dilemma between high activity and excellet stability in acid water splitting, which is expected to be further extended to other electrocatalyst design and synthesis.

Methods

Materials. Iridium(III) 2,4-pentanedionate ($Ir(acac)_3$, Sigma-Aldrich (Shanghai) Trading Co., Ltd. China, 97%), Palladium (Ⅱ) acetylacetonate ($Pd(acac)_2$, Sigma-Aldrich (Shanghai) Trading Co., Ltd. China, 99%), Rhodium(III)2,4-pentanedionate ($Rh(acac)_3$, Sigma-Aldrich (Shanghai) Trading Co., Ltd. China, 97%), Molybdenumhexacarbonyl ($Mo(CO)_6$, 98%), $W(CO)_6$, Oleylamine (Sigma-Aldrich (Shanghai) Trading Co., Ltd. China, technical grade 70%). Nafion solution (5%) was purchased from Sigma-Aldrich. The deionized water is ultrapure water (18.2 MΩ·cm) in all experiments.

Preparation of IrPdRhMoW HEA nanoparticles. $Ir(acac)_3$ (10.0 mg), $Pd(acac)_2$ (10.0 mg), $Rh(acac)_3$ (10.0 mg), $Mo(CO)_6$ (50.0 mg) and $W(CO)_6$ (50.0 mg) with oleylamine (5 mL) were added into a vial. Then the vial was capped and sonicated for 30 minutes to get a transparent solution. The vial was heated to 160 °C from room temperature, and then kept at this temperature for 8 h under magnetic stirring. The black colloidal products were collected by centrifugation and washed two or three times with ethanol/cyclohexane mixture before they were naturally cooled to temperature.

Characterization. TEM and HRTEM on a JEM-2100UHR at an accelerating voltage of 200 KV were used to characterize the morphologies of the samples. XRD spectra were recorded on an X'Pert-Pro MPD diffractometer (Netherlands PANalytical) operating at 40 KV and 40 mA with Cu Kα radiation. XPS were collected with a VG ESCALABMK II spectrometer. H_2 content was analyzed by gas chromatography (GC-7890B, Agilent, America, TCD, with MS-5 Å molecular sieve column and Ar as a carrier gas). AFM analysis was performed using Asylum Research, MFP-3D-BIO. The compositions of catalysts were determined by the ICP-AES (Varian 710-ES).

Electrochemical measurements. Before the electrochemical tests, the as-prepared catalysts were dispersed in a mixture of isopropanol + ultrapure water + 5% Nafion (v:v:v=3:1:0.05) with a concentration of 1 mg mL^{-1}. All the electrochemical tests were conducted by CHI760E electrochemical workstation

(Chenhua, Shanghai) with a traditional three-electrode system. The catalysts modified glass carbon electrode (GCE) was used as working electrode, a carbon rod was used as counter electrode, and a saturated calomel electrode (SCE) was used as reference electrode. The potential was calibrated by the Nernst equation that $E_{RHE} = E_{SCE} + 0.242 + 0.0592$ pH. Before each test, GCE was polished by Al_2O_3 powder to get a smooth surface. And take 10 μL of the mixed slurry and drop it evenly on the surface of the GCE, after it is naturally dried, further electrochemical tests are performed. The HER and OER performance were tested in N_2 and O_2-saturated 0.5 M H_2SO_4. Before every test, the catalyst modified GCE was activating by cycling at -0.2 V-1.1 V *vs.* RHE at 500 mV s^{-1} for 100 cycles. The polarization curves were conducted at a scan rate of 5 mV s^{-1} with 95 % iR compensation. The durability test was performed in 0.5 M H_2SO_4 solution using chronoamperometry. In addition, the LSV after 10000 cycles of CV was measured to further evaluate the stability of the catalyst. EIS measurement was performed at a frequency of 0.1 Hz to 100 kHz in a 0.5 M H_2SO_4 solution.

Thermodynamic Calculations. When the composition atomic radius difference $\delta > 6.5\%$, at the same time, the more negative the mixing enthalpy of the alloy system, the more favorable for the formation of the amorphous phase.

$$\bar{r} = \sum_{i=1}^{n} C_i r_i \quad (1)$$

$$\delta = \sqrt{\sum_i C_i (1 - \frac{r_i}{\bar{r}})^2} \quad (2)$$

$$\Delta H_{\text{mix}} = \sum_{i=1\ i\neq j}^{n} \Omega_{ij} C_i C_j \quad (3)$$

$$\Omega_{ij} = \Delta H_{ij}^{m_i x} \quad (4)$$

where R is the gas constant, C_i or C_j is the atomic percentage of the i*th* or j*th* component. $H_{ij}^{m_i x}$ is the mixing enthalpy for the binary liquid *ij* alloys.[48]

Computational methods. To investigate the HER and OER performances of IrPdRhMoW HEA, we introduce the DFT calculations based on the CASTEP packages.[49] The generalized gradient approximation (GGA) and Perdew-Burke-Ernzerhof (PBE) functionals have been chosen to achieve accurate and satisfying descriptions of exchange-correlation interactions.[50-52] The plane-wave basis cutoff energy has been set to 380 eV and the ultrasoft pseudopotentials have been applied for all the geometry optimizations based on the Broyden-Fletcher-Goldfarb-Shannon (BFGS) algorithm.[53] Meanwhile, for the k-point settings, we apply the coarse quality for all the energy minimizations based on the balance between computational loadings and accuracy. The IrPdRhMoW HEA has been constructed based on the unit cell

of Pd with six-layer thickness. The ratios of metal elements are consistent with the experimental characterizations. We have introduced 20 Å vacuum space in the z-axis for all the models to guarantee sufficient space for geometry optimizations. In addition, the convergence criteria of the geometry optimizations have been set, where the Hellmann-Feynman forces should be smaller than 0.001 eV/Å, the total energy difference should be smaller than 5×10^{-5} eV/atom, and the inter-ionic displacement should not exceed 0.005 Å.

Corresponding Authors

*(L.W.) E-mail: inorchemwl@126.com.

*(B. H.) E-mail: bhuang@polyu.edu.hk

*(J. L.) E-mail: jplai@qust.edu.cn

Acknowledgment

This work was supported by the National Natural Science Foundation of China (51772162, 22001143, and 52072197), Youth Innovation and Technology Foundation of Shandong Higher Education Institutions, China (2019KJC004), Outstanding Youth Foundation of Shandong Province, China (ZR2019JQ14), Taishan Scholar Young Talent Program (tsqn201909114, tsqn201909123), Natural Science Foundation of Shandong Province (ZR2020YQ34), Major Scientific and Technological Innovation Project (2019JZZY020405), and Major Basic Research Program of Natural Science Foundation of Shandong Province under Grant (ZR2020ZD09).

Author contributions

L.W. and J.L. conceived and supervised the research. J.L. and D.Z. designed the experiments. D.Z. performed the experiments, analyzed the data and wrote the full text. Y.S. checked the format of the article. X. C. revisions to the article. B.H. performed theoretical calculations. All authors discussed the results and commented on the manuscript.

References

1 Lin, C. *et al.* In-situ reconstructed Ru atom array on α-MnO_2 with enhanced performance for acidic water oxidation. *Nat. Catal.* **4**, 1012-1023 (2021).

2 King, L. *et al.* A non-precious metal hydrogen catalyst in a commercial polymer electrolyte membrane electrolyser. *Nat. Nanotech.* **14**, 1071–1074 (2021).

3 Seitz, L *et al.* A highly active and stable IrO/$SrIrO_3$ catalyst for the oxygen evolution reaction *Science* **353**, 1011-1014 (2016).

4 Podjaski, F. *et al.* Rational strain engineering in delafossite oxides for highly efficient hydrogen evolution catalysis in acidic media. *Nat. Catal.* **3**, 55-63 (2020).

5 Wang, H. *et al.* Bifunctional non-noble metal oxide nanoparticle electrocatalysts through lithium-induced conversion for overall water splitting. *Nat. Commun.* **6**, 7261 (2015).

6 Rao, R. R. *et al*. Operando identification of site-dependent water oxidation activity on ruthenium dioxide single-crystal surfaces. *Nat. Catal*. **3**, 516–525 (2020).

7 Ji, X. *et al.* Graphene/MoS_2/$FeCoNi(OH)_x$ and Graphene/MoS_2/$FeCoNiP_x$ multilayer-stacked vertical nanosheets on carbon fibers for highly efficient overall water splitting. *Nat. Commun.* **12**, 1380 (2021).

8 Zhu, J., Hu, L., Zhao, P., Lee, L. Y. S. & Wong, K.-Y. Recent Advances in electrocatalytic hydrogen evolution using nanoparticles. *Chem. Rev.* **120**, 851-918 (2020).

9 Sun, Y *et al.* Modulating electronic structure of metal-organic frameworks by introducing atomically dispersed Ru for efficient hydrogen evolution. *Nat. Commun.* **12**, 1369 (2021).

10 Shan, J., Zheng, Y., Shi, B., Davey, K. & Qiao, S.-Z. Regulating electrocatalysts via surface and interface engineering for acidic water electrooxidation. *ACS Energy Lett.* **4**, 2719-2730 (2019).

11 Liu, Y. *et al.* Iridium-containing water-oxidation catalysts in acidic electrolyte. *Chin. J. Catal.* **42**, 1054-1077 (2021).

12 Wang, J. *et al.* Amorphization activated ruthenium-tellurium nanorods for efficient water splitting. *Nat. Commun.* **10**, 5692 (2019).

13 Wang, H. *et al.* Significantly enhanced overall water splitting performance by partial oxidation of Ir through Au modification in core–shell alloy structure. *J. Am. Chem. Soc.* **143**, 4639–4645 (2021).

14 Zhu, J. *et al.* Regulative electronic states around ruthenium/ruthenium disulphide heterointerfaces for efficient water splitting in acidic media. *Angew. Chem. Int. Ed.* **60**, 12328-12334 (2021).

15 Yu, J. *et al.* Ru–Ru_2PΦNPC and NPC@RuO_2 synthesized via environment-friendly and solid-phase phosphating process by saccharomycetes as N/P sources and carbon template for overall water splitting in acid electrolyte. *Adv. Funct. Mater.* **29**, 1901154 (2019).

16 Huang, X. Channel rich RuCu nanosheets for pH-universal overall water splitting electrocatalysis. *Angew. Chem. Int. Ed.* **58**, 13983-13988 (2019).

17 Zhang, L. *et al.* $SrIrO_3$ modified with laminar Sr_2IrO_4 as a robust bifunctional electrocatalyst for overall water splitting in acidic media. *Chem. Eng. J.* **419**, 129604 (2021).
18 Li, L. *et al.* Electrochemically modifying the electronic structure of IrO_2 nanoparticles for overall electrochemical water splitting with extensive adaptability. *Adv. Energy Mater.* **10**, 2001600 (2020).
19 Liu, J. *et al.* Self-supported hierarchical IrO_2@NiO nanoflake arrays as an efficient and durable catalyst for electrochemical oxygen evolution. *ACS Appl. Mater. Interfaces* **11**, 25854-25862 (2019).
20 Hao, S. *et al.* Torsion strained iridium oxide for efficient acidic water oxidation in proton exchange membrane electrolyzers. *Nat. Nanotechnol.* **16**, 1371–1377 (2021).
21 Kibsgaard, J. & Chorkendorff, I. Considerations for the scaling-up of water splitting catalysts. *Nat. Energy* **4**, 430-433 (2019).
22 Bessarabov, D. *et al.* Gas crossover mitigation in PEM water electrolysis: hydrogen cross-over benchmark study of 3M's Ir-NSTF based electrolysis catalyst-coated membranes. *ECS Trans.* **75**, 1165-1173 (2016).
23 Zhan, C. *et al.* Subnanometer high-entropy alloy nanowires enable remarkable hydrogen oxidation catalysis. *Nat. Commun.* **12**, 6261 (2021).
24 Marques, F. *et al.* Review and outlook on high-entropy alloys for hydrogen storage. *Energy Environ. Sci.* **14**, 5191-5227 (2021).
25 Zhang, D. *et al.* Multi-site electrocatalysts boost pH-universal nitrogen reduction by high-entropy alloys. *Adv. Funct. Mater.* **31**, 2006939 (2020).
26 Li, H. *et al.* Fast site-to-site electron transfer of high-entropy alloy nanocatalyst driving redox electrocatalysis. *Nat. Commun.* **11**, 5437 (2020).
27 Pedersen, J. K. *et al.* Bayesian optimization of high-entropy alloy compositions for electrocatalytic oxygen reduction. *Angew. Chem. Int. Ed.* **60**, 24144-24152 (2021).
28 Qiao, H. *et al.* A high-entropy phosphate catalyst for oxygen evolution reaction. *Nano Energy* **86**, 106029 (2021).
29 Mori, K. *et al.* Hydrogen spillover-driven synthesis of high-entropy alloy nanoparticles as a robust catalyst for CO_2 hydrogenation. *Nat. Commun.* **12**, 3884 (2021).
30 Li, T. *et al.* Denary oxide nanoparticles as highly stable catalysts for methane combustion. *Nat. Catal.* **4**, 62–70 (2021).
31 Zhang, L. *et al.* Sodium-decorated amorphous/crystalline RuO_2 with rich oxygen vacancies: A robust pH-universal oxygen evolution electrocatalyst. *Angew. Chem. Int. Ed.* **60**, 18821-18829 (2021).

32 Chen, Y. *et al.* Phase engineering of nanomaterials. *Nat. Rev. Chem.***4**, 243-256 (2020).
33 Yu, S.-H. *et al.* Scale-up synthesis of amorphous NiFeMo oxides and their rapid surface reconstruction for superior oxygen evolution catalysis. *Angew. Chem. Int. Ed.* **58**, 15772-15777 (2019).
34 Ge, J. *et al.* Ultrathin amorphous/crystalline heterophase Rh and Rh alloy nanosheets as tandem catalysts for direct indole synthesis. *Adv. Mater.* **33**, 2006711 (2021).
35 Kuang, M. *et al.* Amorphous/crystalline heterostructured cobalt-vanadium-iron (oxy)hydroxides for highly efficient oxygen evolution reaction. *Adv. Energy Mater.* **10**, 2002215 (2020).
36 Chen, M. *et al.* Zn-VO_x-Co nanosheets with amorphous/crystalline heterostructure for highly efficient hydrogen evolution reaction. *Chem. Eng. J.* **432**, 134329 (2021).
37 Anantharaj, S. & Noda, S. Amorphous catalysts and electrochemical water splitting: An untold story of harmony. *Small* **16**, 1905779 (2020).
38 Fan, J. *et al.* Hydrogen stabilized RhPdH 2D bimetallene nanosheets for efficient alkaline hydrogen evolution. *J. Am. Chem. Soc.* **142**, 3645-3651 (2020).
39 Yu, H. *et al.* Defect-rich porous Pd metallene for enhanced alkaline oxygen reduction electrocatalysis. *Angew. Chem. Int. Ed.* **60**, 12027-12031 (2021).
40 Prabhu, P. & Lee, J.-M. Metallenes as functional materials in electrocatalysis. *Chem. Soc. Rev.* **50**, 6700-6719 (2021).
41 Mu, X. *et al.* RuRh bimetallene nanoring as high-efficiency pH-universal catalyst for hydrogen evolution reaction. *Adv. Sci.* **8**, 2002341 (2022).
42 Luo, M. *et al.* PdMo bimetallene for oxygen reduction catalysis. *Nature* **574**, 81-85 (2019).
43 Dang, Q. *et al.* Iridium metallene oxide for acidic oxygen evolution catalysis. *Nat. Commun.* **12**, 6007 (2021).
44 Zhu, Y., Bu, L., Shao, Q. & Huang, X. Structurally ordered Pt_3Sn nanofibers with highlighted antipoisoning property as efficient ethanol oxidation electrocatalysts. *ACS Catal.* **10**, 3455-3461 (2020).
45 Xie, P. *et al.* Highly efficient decomposition of ammonia using high-entropy alloy catalysts. *Nat. Commun.* **10**, 4011 (2019).
46 Zhu, J. *et al.* Iridium-based cubic nanocages with 1.1-nm-thick-walls: A highly efficient and durable electrocatalyst for water oxidation in an acidic medium. *Angew. Chem. Int. Ed.* **58**, 7244-7248 (2019).

47 Zhao, Y. *et al.* 3D nanoporous iridium-based alloy microwires for efficient oxygen evolution in acidic media. *Nano Energy* **59**, 146-153 (2019).
48 Takeuchi, A. & Inoue, A. Classification of bulk metallic glasses by atomic size difference, heat of mixing and period of constituent elements and its application to characterization of the main alloying element. *Mater. Trans.***46**, 2817-2829 (2005).
49 Clark, S. J. *et al.* First principles methods using CASTEP. *Z. Kristallogr.* **220**, 567-570 (2005).
50 Perdew, J. P., Burke, K. & Ernzerhof, M. Generalized gradient approximation made simple. *Phys. Rev. Lett.* **77**, 3865-3868 (1996).
51 Hasnip, P. J. & Pickard, C. J. Electronic energy minimisation with ultrasoft pseudopotentials. *Comput. Phys. Commun.* **174**, 24-29 (2006).
52 Perdew, J. P. *et al.* Atoms, molecules, solids, and surfaces: Applications of the generalized gradient approximation for exchange and correlation. *Phys. Rev. B* **46**, 6671-6687 (1992).
53 Head, J. D. & Zerner, M. C. A Broyden—Fletcher—Goldfarb—Shanno optimization procedure for molecular geometries. *Chem. Phys. Lett.* **122**, 264-270 (1985).

Figures

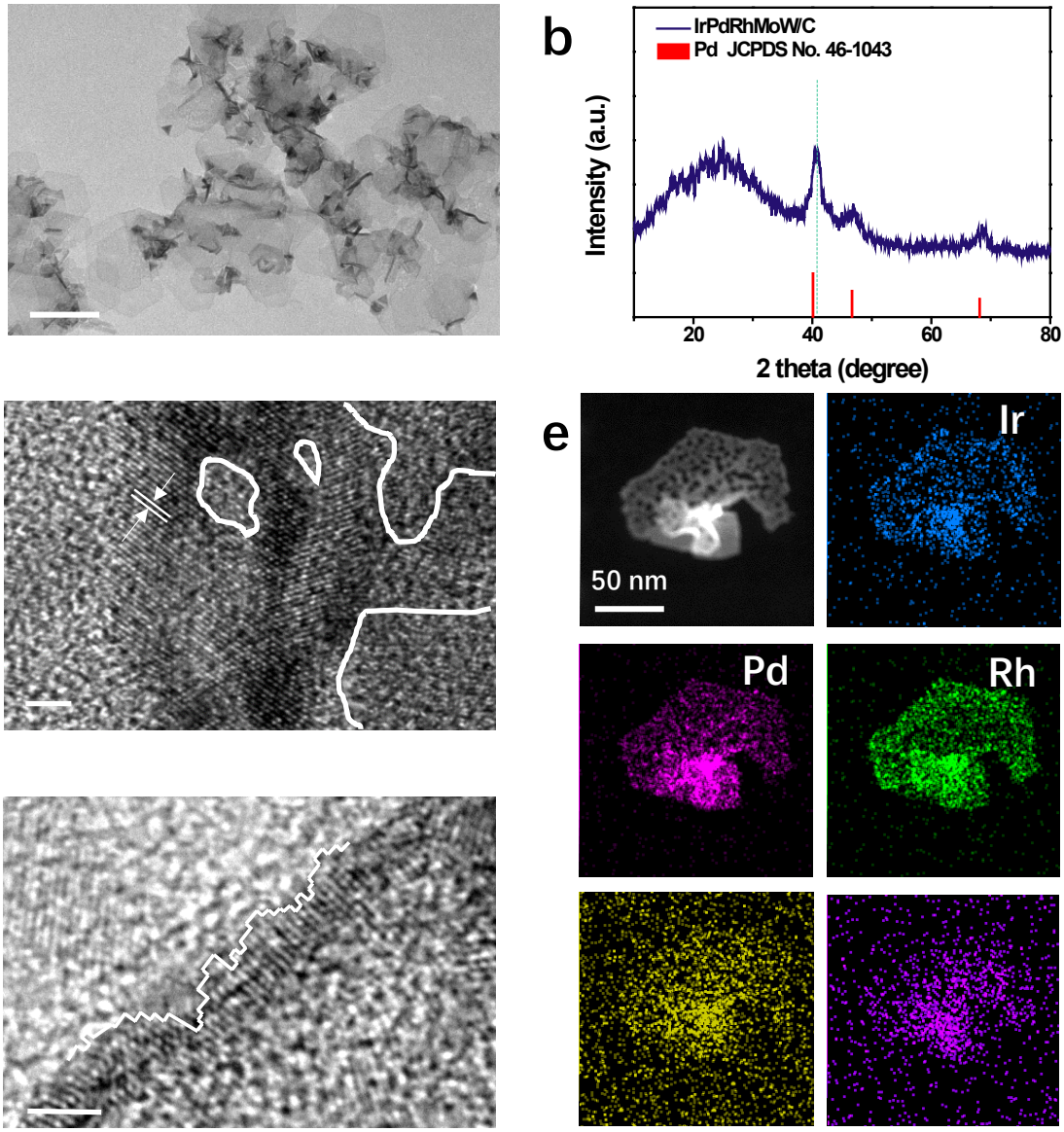

Fig. 1 Structural analyses of the IrPdRhMoW HEA metallene catalysts. (a) TEM image. (b) XRD pattern. (c, d) HRTEM images. (e) HAADF-STEM and corresponding EDX mapping images.

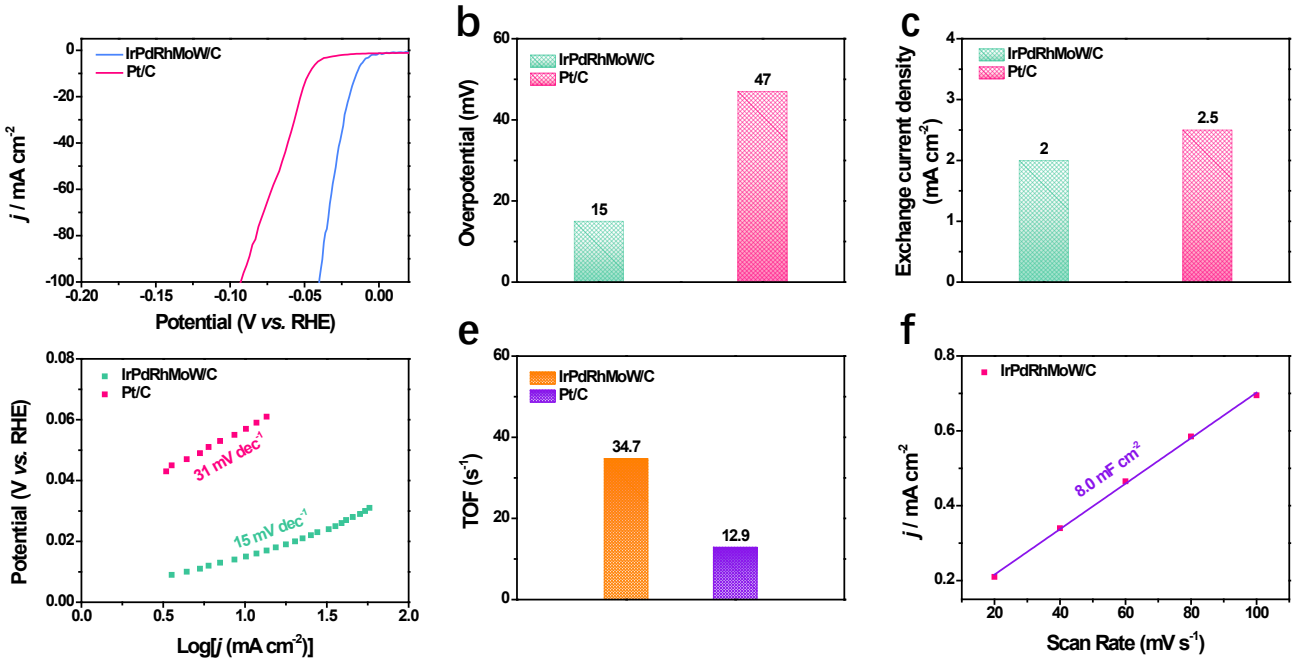

Fig. 2 HER performance of catalysts in 0.5 M H_2SO_4. (a) HER polarization curves, (b) Overpotentials at 10 mA cm^{-2}. (c) Exchange current density. (d) The corresponding Tafel plots. (e) TOF values. (f) Capacitive currents as a function of scan rate of IrPdRhMoW/C.

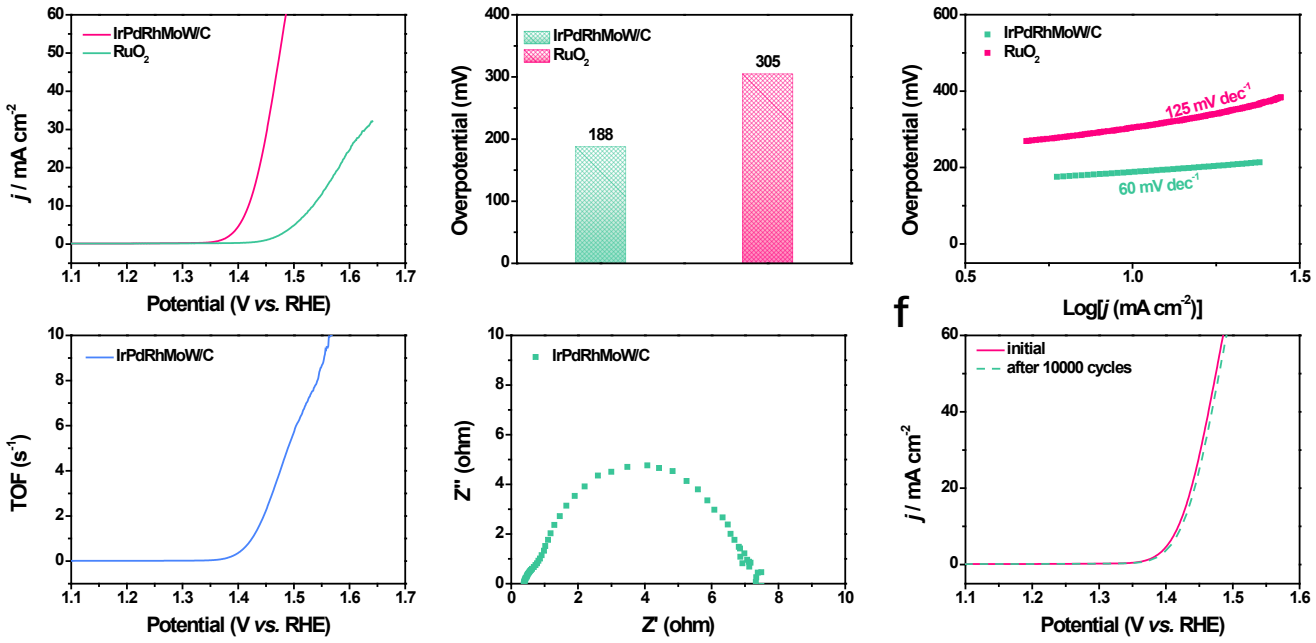

Fig. 3 OER performance of catalysts in 0.5 M H_2SO_4. (a) OER polarization curves. (b) Overpotentials at 10 mA cm^{-2}. (c) The corresponding Tafel plots. (d) TOF values. (e) Electrochemical impedance spectra of IrPdRhMoW/C. (f) Polarization curves of IrPdRhMoW/C before and after 10000 CV cycles.

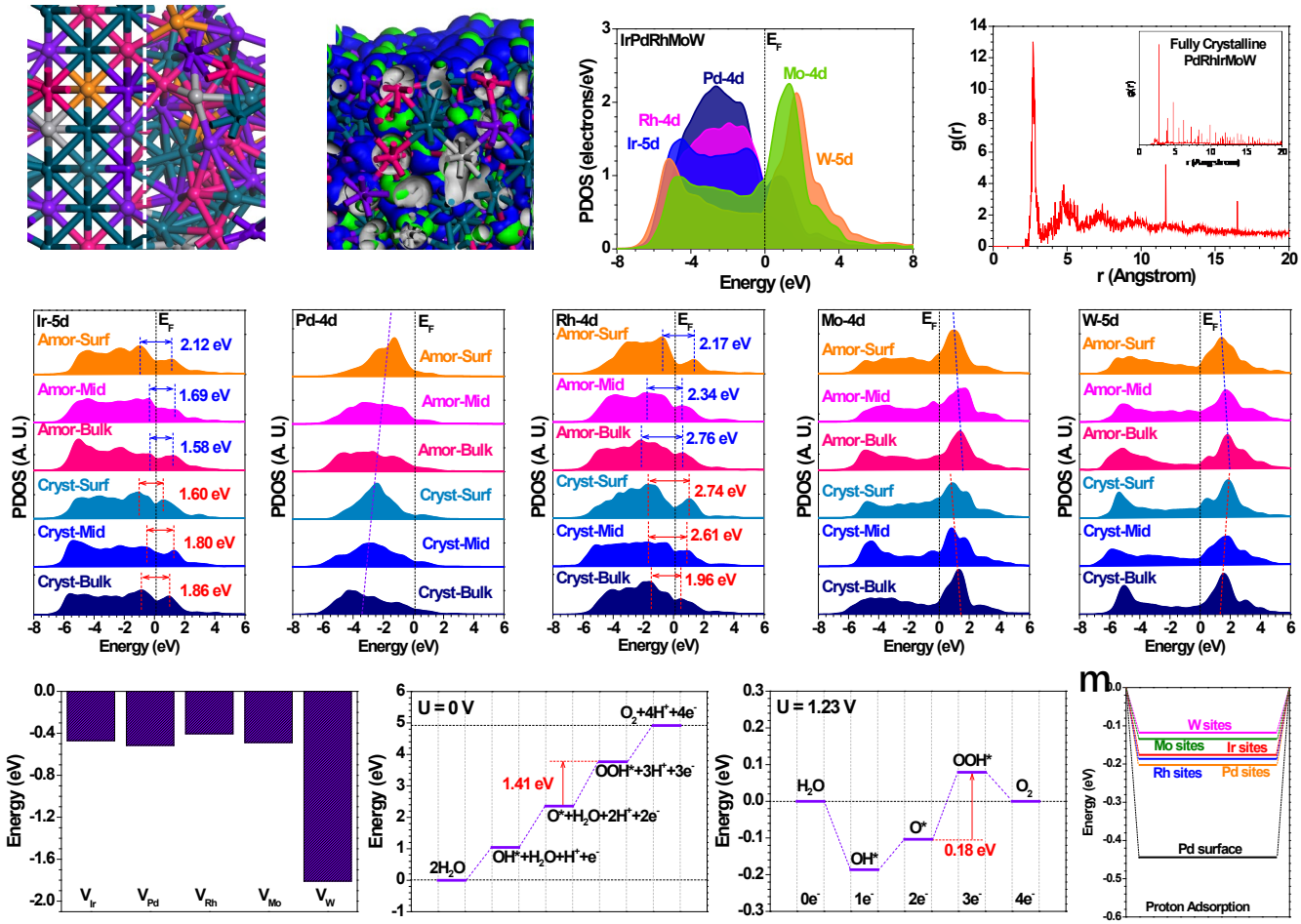

Fig. 4 DFT calculations. (a) The top view of the IrPdRhMoW structure. (b) 3D contour plot of electronic distribution near Fermi level of IrPdRhMoW. Dark green balls = Pd, purple balls = Rh, orange balls = Mo, pink balls = Ir and grey balls = W. Blue isosurface = bonding orbitals and green isosurface = anti-bonding orbitals. (c) The PDOS of IrPdRhMoW HEA. (d) The simulated RDF of IrPdRhMoW HEA. The inset is the RDF of crystalline IrPdRhMoW. The site-dependent PDOS of (e) Ir-5d (f) Pd-4d, (g) Rh-4d, (h) Mo-4d and (i) W-5d. (j) The formation energy of different metal vacancies. (k) The energy change of OER at U = 0 V. (l) The energy change of OER at U = 1.23 V. (m) The binding energy comparisons of the proton.

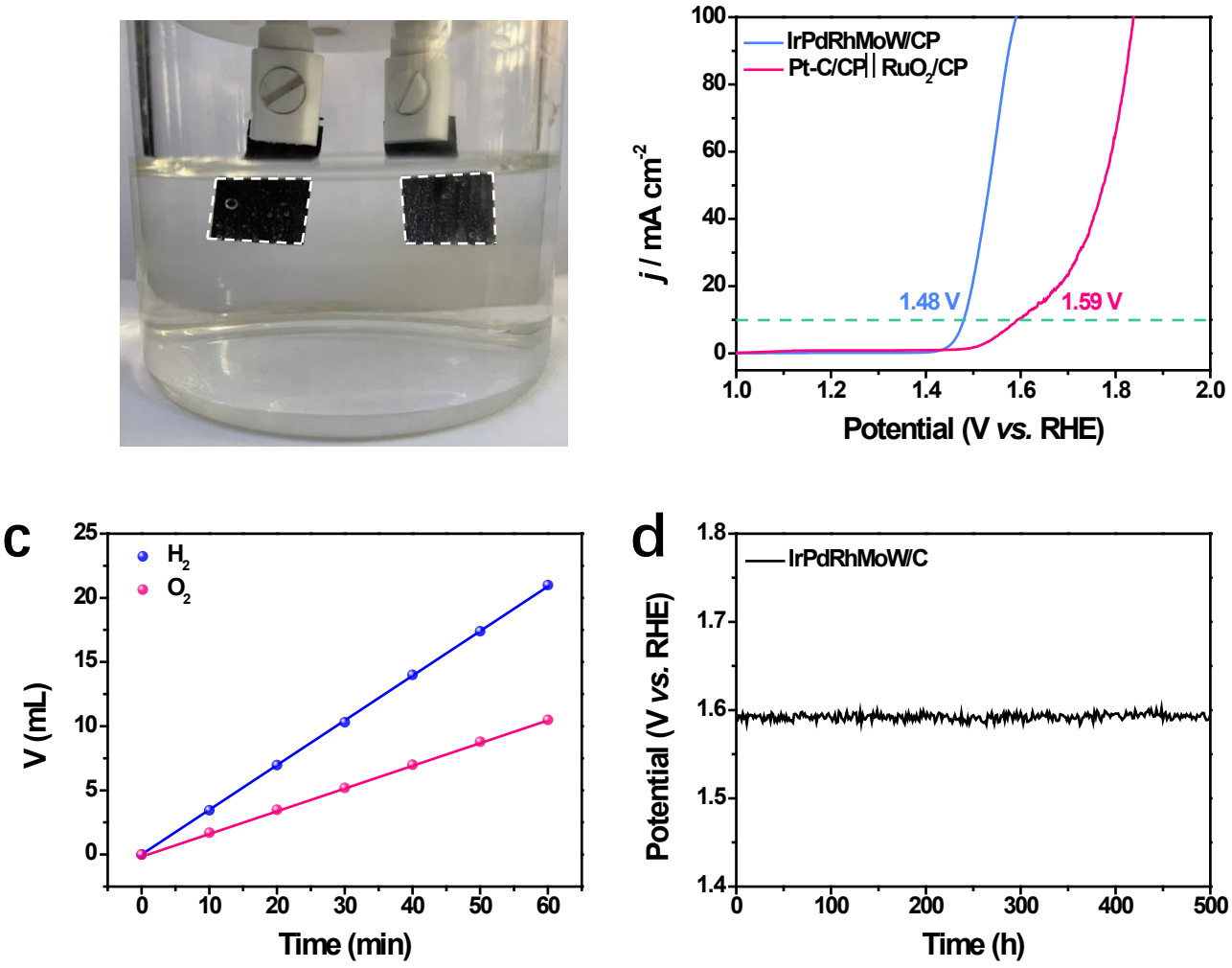

Fig. 5 Overall water-splitting performance of catalysts in 0.5 M H_2SO_4. (a) The digital photo of two-electrode configuration with bubbles on both electrodes. (b) Polarization curves of the two-electrode overall water splitting cells. (c) The amount of H_2 and O_2 theoretically calculated and experimentally measured for IrPdRhMoW/CP||IrPdRhMoW/CP for 60 minutes. (d) Chronopotentiometry curve of IrPdRhMoW/CP||IrPdRhMoW/CP at 100 mA cm^{-2}.